J. Fluid Mech. (2007), *vol.* 584, *pp.* 357–372.
doi:10.1017/S0022112007006428 Printed in the United Kingdom

Variable-density miscible displacements in a vertical Hele-Shaw cell: linear stability

N. GOYAL, H. PICHLER AND E. MEIBURG†

Department of Mechanical Engineering, University of California, Santa Barbara, CA 93106, USA

(Received 14 April 2006 and in revised form 5 March 2007)

A computational study based on the Stokes equations is conducted to investigate the effects of gravitational forces on miscible displacements in vertical Hele-Shaw cells. Nonlinear simulations provide the quasi-steady displacement fronts in the gap of the cell, whose stability to spanwise perturbations is subsequently examined by means of a linear stability analysis. The two-dimensional simulations indicate a marked thickening (thinning) and slowing down (speeding up) of the displacement front for flows stabilized (destabilized) by gravity. For the range investigated, the tip velocity is found to vary linearly with the gravity parameter. Strongly stable density stratifications lead to the emergence of flow patterns with spreading fronts, and to the emergence of a secondary needle-shaped finger, similar to earlier observations for capillary tube flows. In order to investigate the transition between viscously driven and purely gravitational instabilities, a comparison is presented between displacement flows and gravity-driven flows without net displacements.

The linear stability analysis shows that both the growth rate and the dominant wavenumber depend only weakly on the Péclet number. The growth rate varies strongly with the gravity parameter, so that even a moderately stable density stratification can stabilize the displacement. Both the growth rate and the dominant wavelength increase with the viscosity ratio. For unstable density stratifications, the dominant wavelength is nearly independent of the gravity parameter, while it increases strongly for stable density stratifications. Finally, the kinematic wave theory of Lajeunesse *et al.* (*J. Fluid Mech.* vol. 398, 1999, p. 299) is seen to capture the stability limit quite accurately, while the Darcy analysis misses important aspects of the instability.

1. Introduction

Displacements in Hele-Shaw cells are frequently employed to study generic instability phenomena of relevance to a wide range of applications. In one such investigation, Goyal & Meiburg (2006) focus on the viscous fingering instability of neutrally buoyant miscible fluids. They employ Stokes simulations to obtain quasi-steady two-dimensional base states of the flow in the gap, whose stability properties with regard to spanwise perturbations are subsequently analysed by means of a computational linear stability analysis. The authors find dominant wavelengths of the order of three gap widths, which is substantially lower than the value of 5 ± 1 observed experimentally by Lajeunesse *et al.* (1997). However, in these experiments, a lighter less viscous fluid displaces a heavier more viscous one downward in a vertical

† Author to whom correspondence should be addressed: meiburg@engineering.ucsb.edu

Hele-Shaw cell, so that gravitational forces affect the flow. The extent to which these forces are responsible for the observed discrepancy in the dominant wavelength is the primary subject of the present investigation. Lajeunesse *et al.* (1999) furthermore provide a stability criterion in terms of a critical downward displacement velocity, based on a kinematic wave theory involving gap-averaged flow quantities. We will provide a comparison of this criterion with corresponding information derived from a Stokes flow analysis. The configuration of a vertically oriented gap is of particular interest for advanced oil production techniques that employ miscible flooding via hydraulically induced fractures. Such fractures can extend several hundred feet away from the wellbore, and they are usually oriented vertically.

The related problem of variable density and viscosity, miscible displacements in porous media has been analysed in the context of Darcy flows (cf. Bacri, Salin & Yortsos 1992; Manickam & Homsy 1995). Since Hele-Shaw flows frequently serve as models of porous media displacements, it will be of interest to compare respective predictions based on the Stokes and Darcy equations. Earlier investigations had demonstrated considerable differences in this regard (Graf & Meiburg 2002; Goyal & Meiburg 2004, 2006).

Studies of corresponding miscible displacements in capillary tubes are relevant to the present investigation as well. The experiments by Petitjeans & Maxworthy (1996), Kuang, Maxworthy & Petitjeans (2003, 2004), as well as the axisymmetric simulations of Chen & Meiburg (1996), focus on the fraction of the more viscous fluid left behind on the walls of the tube over a range of density and viscosity contrasts. In different parameter regimes, these authors observe different types of axisymmetric flow patterns, among them quasi-steady displacement fronts, and fronts characterized by needle-shaped protrusions. As will be seen below, the present simulations reveal the existence of similar patterns in Hele-Shaw cells.

Section 2 will define the physical problem and provide an overview over the numerical methods employed. Section 3 presents Stokes simulation results for the two-dimensional flow in the gap, and discusses the properties of the quasi-steady base states. Subsequently, the stability properties of these base states with regard to spanwise perturbations will be examined. The findings will be discussed and summarized in § 4.

2. Problem formulation

2.1. *Governing equations*

Figure 1 shows the geometry of the vertical Hele-Shaw cell, with a less viscous fluid 1 displacing a more viscous fluid 2. Either one of these two miscible fluids can be the denser one, thus allowing gravitationally stable or unstable configurations. Additionally, we also consider the purely gravity-driven case without a net displacement. In this situation, the flow develops as a result of a linear instability, with the heavier fluid sinking and the lighter fluid rising up in the Hele-Shaw cell. For small gap widths e, the flow in both of these scenarios is governed by the three-dimensional Stokes equations

$$\nabla \cdot \boldsymbol{u} = 0, \tag{2.1}$$

$$\nabla p = \nabla \cdot \boldsymbol{\tau} + \rho \boldsymbol{g}, \tag{2.2}$$

$$c_t + \boldsymbol{u} \cdot \nabla c = D \nabla^2 c. \tag{2.3}$$

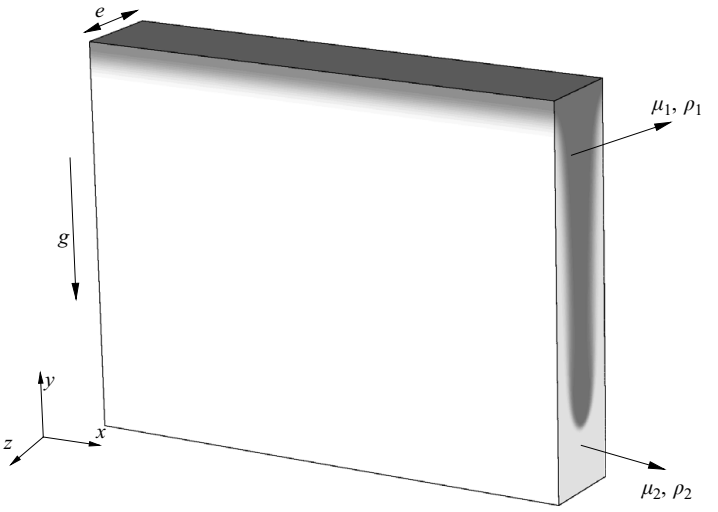

FIGURE 1. Geometry of the vertical Hele-Shaw cell. The less viscous fluid on top displaces the more viscous fluid below.

Here, $\boldsymbol{u}$ denotes the flow velocity, and c indicates the relative concentration of the more viscous fluid. $\boldsymbol{\tau} = \mu(\nabla u + \nabla u^T)$ represents the viscous stress tensor for Newtonian fluids, while D refers to the constant diffusion coefficient. z denotes the gapwise or cross-gap direction, while x will be referred to as the spanwise direction.

Following other authors, the density ρ and the viscosity μ are assumed to be linear and exponential functions of the concentration c, respectively,

$$\rho = \rho_1 - c(\rho_1 - \rho_2) = \rho_1 - c\Delta\rho, \tag{2.4}$$

$$\mu = \mu_2 \exp(R(c-1)), \tag{2.5}$$

$$R = \ln \frac{\mu_2}{\mu_1}, \tag{2.6}$$

where R is the logarithm of the viscosity ratio.

2.2. *Scaling: displacement flows*

When the less viscous fluid is driving out the more viscous one in the downward direction, the governing equations are rendered dimensionless by introducing the characteristic scales

$$L^* = e, \quad U^* = U, \quad T^* = \frac{e}{U}, \quad P^* = \frac{\mu_2 U}{e}, \quad \rho^* = \Delta\rho, \quad \mu^* = \mu_2, \tag{2.7}$$

where U refers to the average velocity across the gap of the Hele-Shaw cell. We thus obtain the set of dimensionless equations as

$$\nabla \cdot \boldsymbol{u} = 0, \tag{2.8}$$

$$\nabla p = \nabla \cdot \boldsymbol{\tau} + Fc\nabla y, \tag{2.9}$$

$$c_t + \boldsymbol{u} \cdot \nabla c = \frac{1}{Pe}\nabla^2 c, \tag{2.10}$$

where

$$Pe = \frac{Ue}{D}, \qquad F = \frac{\Delta\rho\, g\, e^2}{\mu_2 U}. \tag{2.11}$$

The Péclet number Pe indicates the relative strength of convective to diffusive transport, while the gravity number F denotes the ratio of gravitational to viscous forces. A heavier fluid on top results in a positive value of F. Note that an upward displacement with an inverse density stratification is equivalent to the downward flows considered here, so that we can limit our discussion to downward flows without loss of generality.

2.3. *Scaling: gravity driven flows*

In this configuration, the length, density and viscosity scales remain unchanged. In the absence of fluid injection, we define a buoyancy-based velocity, which leads to new scales for time and pressure as well

$$U^* = \frac{\Delta\rho\, g\, e^2}{\mu_2}, \qquad T^* = \frac{\mu_2}{\Delta\rho\, g\, e}, \qquad P^* = \Delta\rho\, g\, e. \tag{2.12}$$

This scaling results in the following form of the dimensionless Stokes equations

$$\nabla\cdot\boldsymbol{u} = 0, \tag{2.13}$$

$$\nabla p = \nabla\cdot\boldsymbol{\tau} + c\nabla y, \tag{2.14}$$

$$c_t + \boldsymbol{u}\cdot\nabla c = \frac{1}{Ra}\nabla^2 c, \tag{2.15}$$

Thus, in the absence of a net flow, the Rayleigh number given by

$$Ra = \frac{\Delta\rho\, g\, e^3}{D\mu_2}. \tag{2.16}$$

represents the ratio of convective to diffusive effects. Note that by setting $F = 1$ in (2.9), and replacing Pe in (2.10) by Ra, we recover (2.14) and (2.15), respectively. Further, we shall employ the fact that

$$Ra = Pe\, F, \tag{2.17}$$

to make quantitative comparisons between the two flows throughout the text.

2.4. *Numerical implementation*

Nonlinear simulations of the Stokes equations in the fourth-order streamfunction formulation are employed to obtain the two-dimensional convectively dominated base states required for the subsequent linear stability analysis. The numerical approach for the neutrally buoyant case is described in detail in Goyal & Meiburg (2006), and the incorporation of the gravity term is straightforward. Once the two-dimensional quasi-steady flow field is obtained from the direct numerical simulation, we perform a linear stability analysis of this base state with regard to periodic perturbations in the spanwise direction. Towards this end, the three-dimensional Stokes equations are linearized around the aforementioned two-dimensional base state, and subsequently discretized to give a generalized eigenvalue problem. To avoid repetition, see our earlier work (Goyal & Meiburg 2006) for details of the numerical implementation, solution methodology and convergence checks. Our goal is to determine the eigenvalue

$$\sigma = f(\beta, Pe, R, F) \tag{2.18}$$

representing the growth rate of the perturbation, along with the associated eigenfunctions. The viscosity ratio R, the Péclet number Pe, and the gravity number F represent the three dimensionless parameters that characterize the base flow, while β reflects the perturbation wavenumber. The solution methodology for the gravity-driven flow is equivalent to that for the displacement flow.

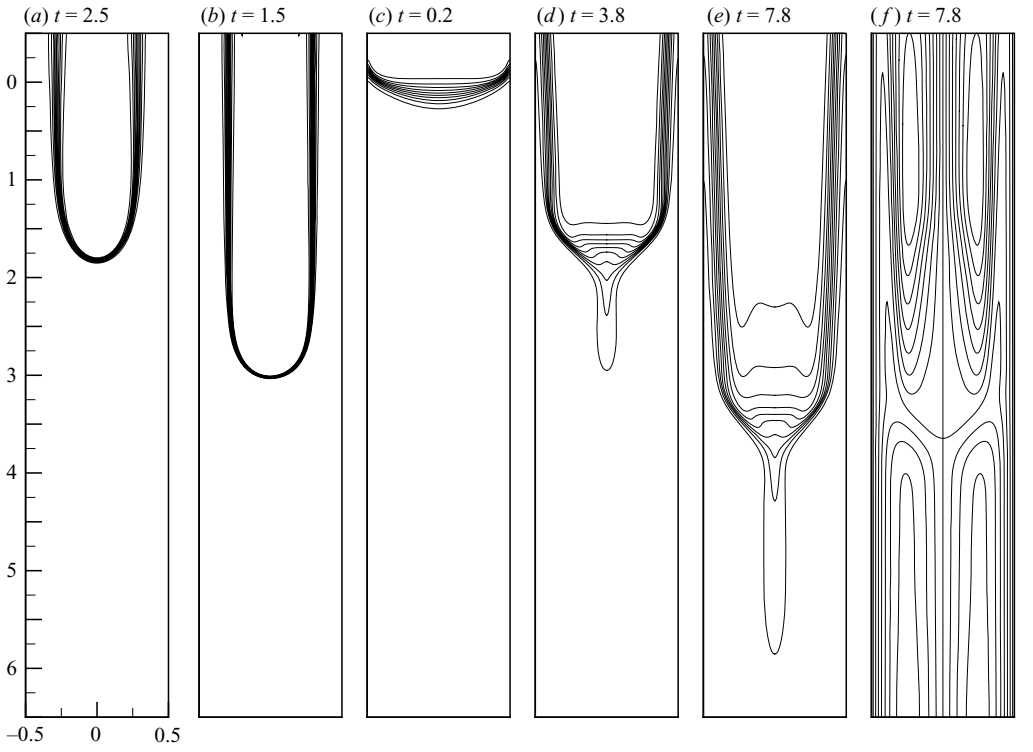

FIGURE 2. Displacement flows: base state concentration fields for $Pe = 2000$, $R = 5$ and (a) $F = 0$, (b) $F = 100$. (c)–(e) Evolution of the 'spike' for $F = -100$. (f) Streamline pattern in a reference frame moving with the $c = 0.5$ contour in (e).

3. Results

3.1. *Two-dimensional simulations: displacement flows*

In Goyal & Meiburg (2006), we characterized the two-dimensional quasi-steady base state by the thickness of the displacement front and its tip velocity. The front thickness d_0 was defined as the distance over which the concentration at the tip of the quasi-steady front changes from 0.1 to 0.9, while the tip velocity is evaluated as the propagation velocity of the $c = 0.5$ contour along the centreline of the cell.

Figures 2(a) and 2(b) show representative base states for $Pe = 2000$, $R = 5$ and $F = 0$ and 100, respectively. Clearly, the evolution of the two-dimensional displacement front is modified by the presence of gravitational effects. Figures 3(a) and 3(b) depict the variation of d_0 and V_{tip}, respectively, with the gravity number for $Pe = 2000$ and different viscosity ratios. An increase in F corresponds to increasingly unstable density stratifications, which result in higher tip velocities and hence thinner fronts. Over the entire range of F considered here, the V_{tip}, F-relationship follows an approximate straight line for all viscosity ratios. In capillary tube experiments, Petitjeans & Maxworthy (1996) observed a similar linear variation for comparable values of F and Pe.

For neutrally buoyant fluids we had found the front thickness to scale with $Pe^{-1/2}$ (Goyal & Meiburg 2006). Gravity forces are found not to alter this scaling for the present range of F-values. At higher viscosity contrasts, the tip velocity is seen to decrease with increasing Pe for all gravity numbers (not shown), in line with earlier

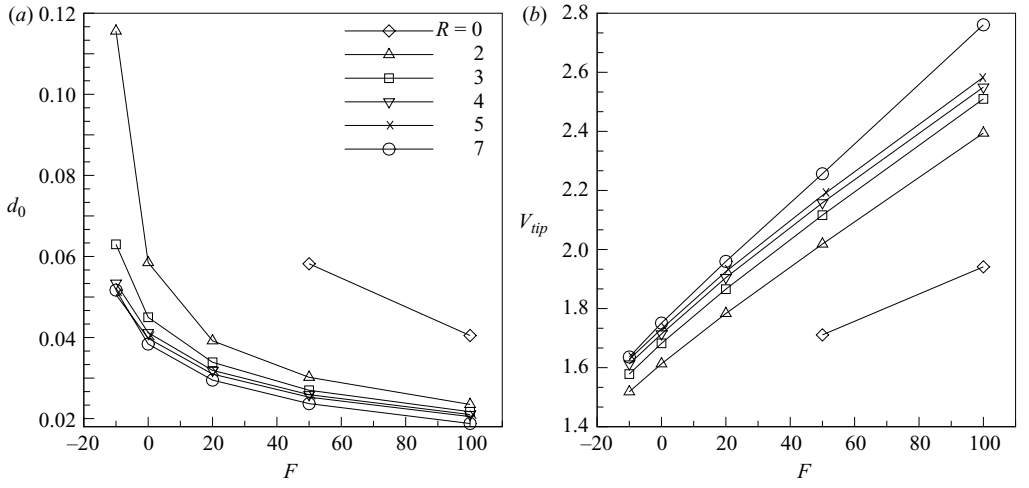

FIGURE 3. (*a*) Tip thickness and (*b*) velocity of the quasi-steady displacement front as a function of F for different viscosity ratios and $Pe = 2000$.

observations by Goyal & Meiburg (2006) for the neutrally buoyant case. This result is in contrast to the experimental findings of Petitjeans & Maxworthy (1996) for capillary tube displacements. In Goyal & Meiburg (2006), we were able to show that this discrepancy is due to the assumption of an exponential viscosity–concentration relationship. For a linear viscosity–concentration relationship, the tip velocity always increases with Pe.

A favourable (stabilizing) density contrast ($F < 0$) slows the front down and thereby reduces the strain field at the finger tip, which results in an increased front thickness. Thus, beyond a transitional range of gravity numbers, a steep concentration front cannot be maintained at the tip, and a quasi-steady state does not develop. In the present study, for $Pe = 2000$ and $F < -10$ different flow fields emerged, depending on the value of R. These flow patterns are qualitatively similar to those observed in the capillary tube investigations of Chen & Meiburg (1996), Petitjeans & Maxworthy (1996) and Kuang *et al.* (2004) and in the theoretical predictions of Lajeunesse *et al.* (1999) for Hele-Shaw cells.

Lajeunesse *et al.* (1999) studied the downward displacement of a heavier miscible fluid by a lighter less viscous one in a Hele-Shaw cell at high flow rates. Their gap-averaged self-similar concentration profiles displayed features of kinematic waves, which prompted them to use kinematic wave theory to obtain a theoretical description of the flow in the gap of the cell. Yang & Yortsos (1997) had proposed a similar asymptotic method for analysing neutrally buoyant two-dimensional Hele-Shaw flows in the limits of infinite Péclet number and large aspect ratios. Under these conditions the flow away from the tip reduces to a parallel flow between two plates, and it can be described by a conservation equation for the gap-averaged concentration. This gap-averaged version of (2.3) takes the hyperbolic form

$$\frac{\partial \bar{C}(y,t)}{\partial t} + \frac{\partial F(y,t)}{\partial y} = 0, \tag{3.1}$$

where

$$\bar{C}(y,t) = \int_{-0.5}^{0.5} c(y,z,t)\,\mathrm{d}z, \tag{3.2}$$

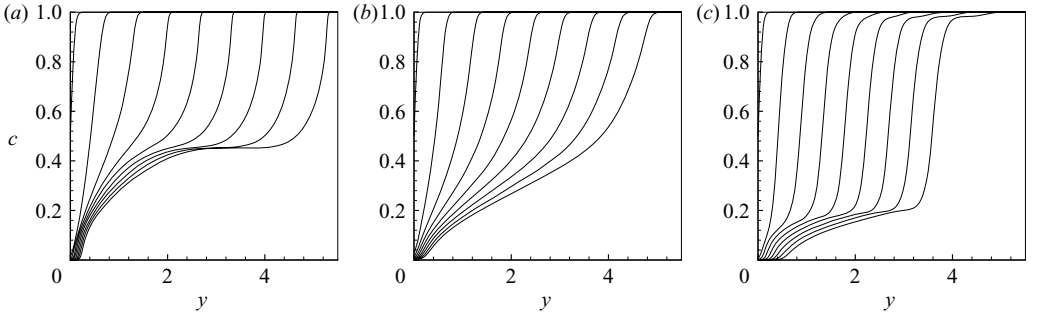

FIGURE 4. Simulation data for the gap-averaged concentration of the less viscous fluid as a function of the streamwise distance for $t = 0, 0.4, 0.8, \ldots, 3.2$, $Pe = 2000$ and (*a*) $F = -10$, $R = 7$, (*b*) $F = -10$, $R = 1$ and (*c*) $F = -100$, $R = 5$.

$$F(y, t) = \int_{-0.5}^{0.5} c(y, z, t)v(y, z, t)\,\mathrm{d}z, \tag{3.3}$$

are the gap-averaged concentration and the mass flux of the more viscous fluid, respectively. Thus the convective velocity of each concentration value $\bar{C}$ depends on the shape of the flux function $F(\bar{C})$ and is given by

$$V(\bar{C}) = \frac{\mathrm{d}F}{\mathrm{d}\bar{C}}. \tag{3.4}$$

A closed-form expression for the streamwise velocity component can then be derived as a function of the specific viscosity–concentration relationship. By assuming a step profile for the viscosity across the interface, the above authors obtain explicit expressions for the flux function $F(\bar{C})$ in terms of the viscosity ratio and $\bar{C}$. By using kinematic wave theory, Lajeunesse *et al.* (1999) predict a critical flow velocity above which the flow becomes unstable and assumes a three-dimensional nature. This will be discussed in more detail in § 3.3. In our case, both the Péclet number and the aspect ratio are finite, and the viscosity varies exponentially with the concentration. Nevertheless, for large Pe we showed in Goyal & Meiburg (2006) that this approach still provides accurate descriptions of the tip velocities and the agreement with the theoretical predictions. The simulation results were seen to improve with increasing Pe. The good comparison between the theoretically predicted tip velocities and the simulation results continues to hold for the flows with a density stratification considered here. Goyal & Meiburg (2006) for a more detailed description of the comparison of the tip velocities from full Stokes simulations with the predictions of the kinematic wave description of Hele-Shaw flows.

Using the above approach in conjuction with their experimental data, Lajeunesse *et al.* (1999) also delineate three distinct flow regimes in the (R, F)-plane, all of which are present in our present simulations. Figure 4 plots the evolution of the gap-averaged concentration for three different parameter combinations to demonstrate the excellent qualitative agreement with the corresponding experimental observations of Lajeunesse *et al.* (1999). The quasi-steady states in our simulations correspond to their regime 3 with frontal shocks. In figure 4(*a*), the propagation of this frontal shock with a constant velocity greater than the maximum Poiseuille flow velocity of 1.5, as the gap-averaged concentration field evolves in time, is distinctly evident. This holds true for all higher values of the gravity parameter as well, whenever a quasi-steady concentration field develops. For small viscosity ratios and mildly negative values

of F, the self-spreading profiles of regime 1 are recovered (figure 4*b*), with the tip moving with the maximum Poiseuille flow velocity.

Finally, figure 4(*c*) shows that for strongly stabilizing density contrasts, self-spreading segments both ahead of and behind an internal shock are observed in our simulations, corresponding to regime 2 in Lajeunesse *et al.* (1999). The concentration fields at different times corresponding to this parameter set ($F = -100$, $Pe = 2000$ and $R = 5$) are shown in figure 2(*c–e*). We observe the emergence of a 'spike-like' structure, with a continuous leakage of the less viscous fluid into the more viscous one. This secondary, needle-shaped finger is characterized by a main finger front advancing more slowly than the maximum velocity of the Poiseuille flow profile far ahead of the finger. The corresponding streamline pattern in a reference frame moving with the tip of the main finger is shown in figure 2(*f*). See Petitjeans & Maxworthy (1996), Chen & Meiburg (1996) and Kuang *et al.* (2004) for a detailed discussion of this streamline pattern. Similar spike structures also evolve for favourable viscosity contrasts, as long as gravity exerts a stabilizing influence (Balasubramaniam *et al.* 2005).

3.2. *Two-dimensional simulations: gravity-driven flows*

This section describes simulations of purely gravity-driven flows without net displacement. We impose a small initial perturbation at the interface between the two fluids, in order to accelerate the evolution of the flow. Depending on the symmetry of this perturbation, different transient flow configurations can result (cf. Fernandez *et al.* 2002). We impose perturbations that are symmetric to the gap centreline, in order to obtain fronts that can be compared to those evolving in displacement flows. The temporal evolution of the concentration field for $Ra = 10^5$ and $R = 0$ is depicted in figures 5(*a*)–5(*e*). The heavier fluid sinks in the centre of the cell, while the lighter fluid rises on both sides of the central downward-moving front. Hence, the velocity vectors in figure 5(*f*) corresponding to the concentration field in figure 5(*e*) show the existence of a substantial reverse flow region which is absent in flows with fluid injection. Similar to the case with fluid injection, for Rayleigh numbers exceeding a certain R-dependent threshold a quasi-steady front evolves. Thus, for $Ra > 10^4$, quasi-steady flow fields were usually seen to develop. Figure 6 plots the gap-averaged concentration at different times for the flow field depicted in figure 5. Similarly to the displacement flows, we observe the evolution of a quasi-steady front propagating with constant velocity in the gap of the cell. A bulging of the front just behind the tip (cf. figure 5*e*) leads to the non-monotonic average concentration profile in figure 6. This effect is exhibited by displacement flows as well (cf. figure 4*a*) and becomes more pronounced with increasing viscosity contrasts. At higher viscosity contrasts, the steady two-dimensional fronts have shapes that are very similar to their net displacement counterparts.

The characteristics of the gravity-driven fronts depend on the governing parameters Ra and R, similarly to the dependence of displacement fronts on F, Pe and R. Figure 7 shows the front thickness and velocity as a function of R for both a purely gravity-driven flow and a comparable displacement flow. For the gravity driven flow, $Ra = 10^5$. To allow a quantitative comparison, we chose the values $Pe = 2000$, $F = 50$ for the displacement flow, so that $Pe\,F = Ra$, cf. (2.17). In order to make a quantitative comparison between the front velocities for the two cases, we furthermore rescale the velocity of the gravity-driven flow using the relation between the characteristic velocity scales for the two situations

$$U^*_{displacement}/U^*_{gravity} = F. \tag{3.5}$$

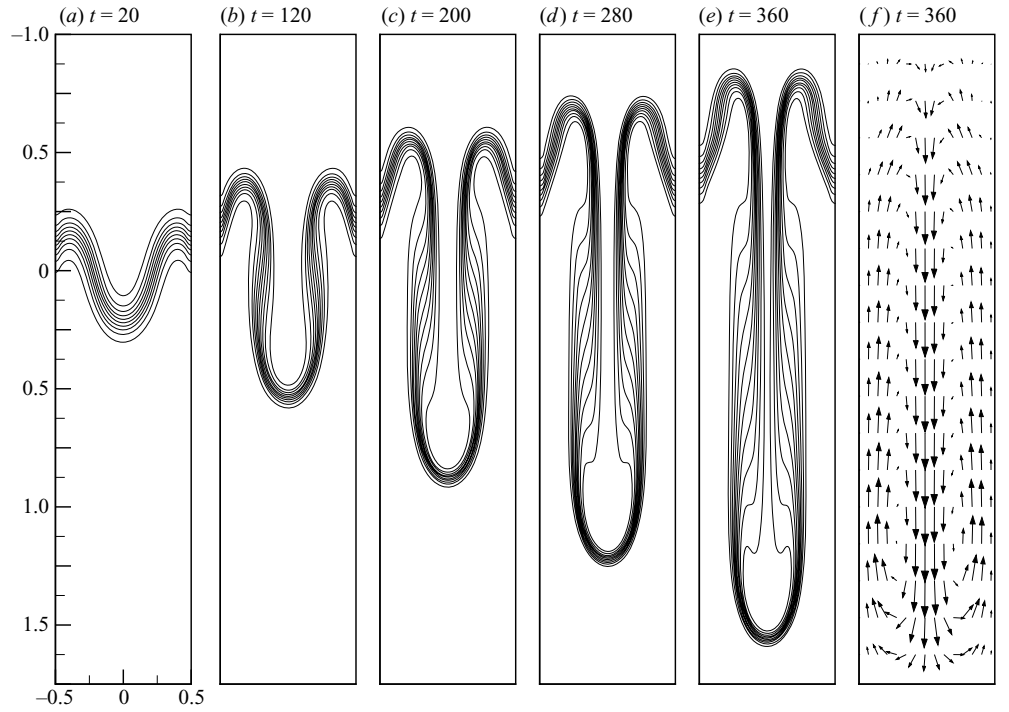

FIGURE 5. Gravity-driven flow. (*a–d*) Evolution of the quasi-steady base state for $Ra = 10^5$ and $R = 0$. (*e*) Velocity vectors of the quasi-steady state.

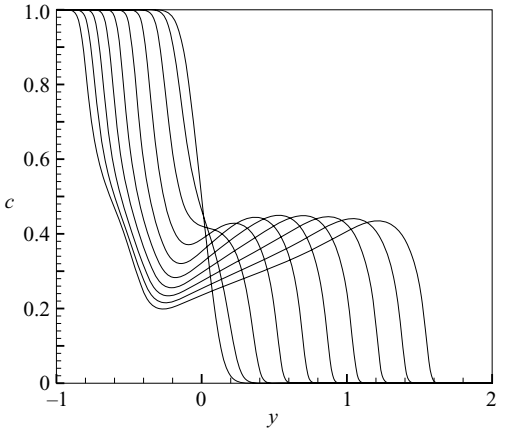

FIGURE 6. Gravity-driven flow. Gap-averaged concentration profiles for $t = 0, 40, 80, \ldots, 360$, $Ra = 10^5$ and $R = 0$.

In addition, we subtract out the displacement velocity along the centreline for the displacement flow, so that figure 7(*b*) plots $(V_{tip} - 1.5)$ for the $Pe = 2000$ and $F = 50$ simulation. The similarities between the two cases become apparent immediately from figure 7. The front thickness decreases, while the tip velocity increases with R for all flows. In addition, we find d_0 to scale with $Ra^{-0.5}$ (not shown), akin to the corresponding scaling with Pe in displacement flows. For $R = 0$, since only gravitational effects are present, d_0 and V_{tip} have almost identical values in both

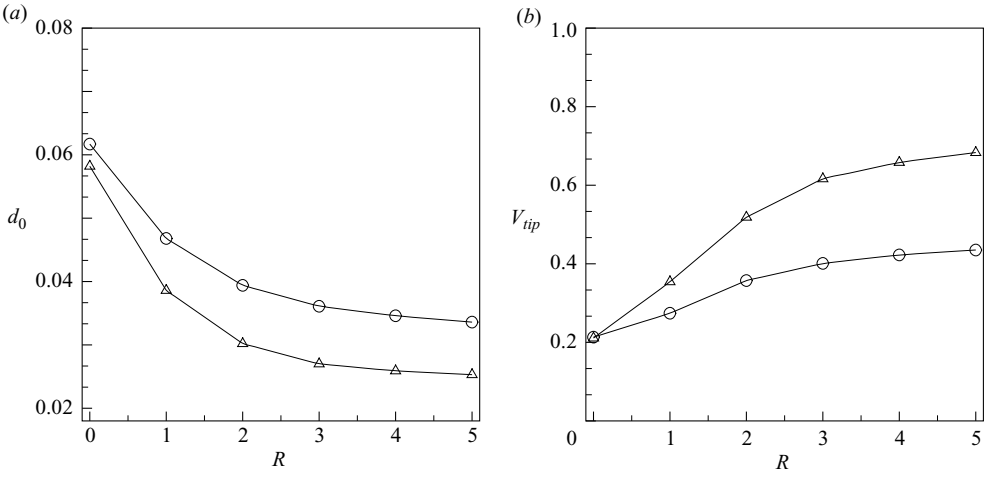

FIGURE 7. Comparison between the variation of (*a*) the tip thickness and (*b*) the velocity of the quasi-steady fronts with R, with and without fluid injection. ○, $Ra = 10^5$; △, $F = 50$, $Pe = 2000$.

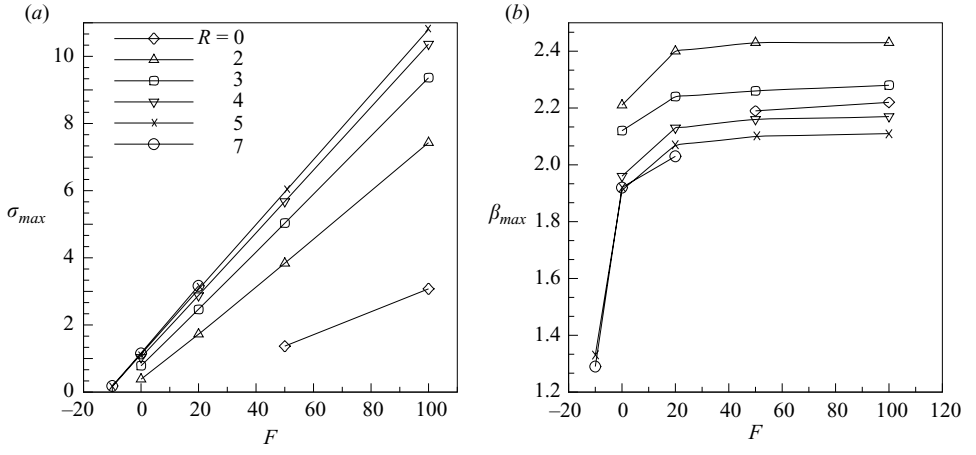

FIGURE 8. (*a*) Growth rate and (*b*) most unstable wavenumber as a function of F for different viscosity ratios and $Pe = 2000$.

flow configurations. An increase in R strengthens the viscous effects relative to the gravitational ones, so that the displacement flows show a stronger dependence on R. In their experimental study of gravitationally unstable flows in capillary tubes without net displacement, Kuang *et al.* (2004) make similar observations regarding the velocity of the front.

3.3. *Linear stability*

Figure 8(*a*) shows the maximum growth rate σ_{max} as a function of the gravity number F, for $Pe = 2000$ and different viscosity ratios. Gravitational forces are seen to have a strong influence on the growth rate, so that even moderately negative values of F can completely stabilize the displacement. Thus, for $R \leqslant 4$, a value of $F = -10$ suffices to produce a stable displacement. For even lower values of F, a quasi-steady state no longer develops, so that a linear stability analysis cannot be performed. Conversely,

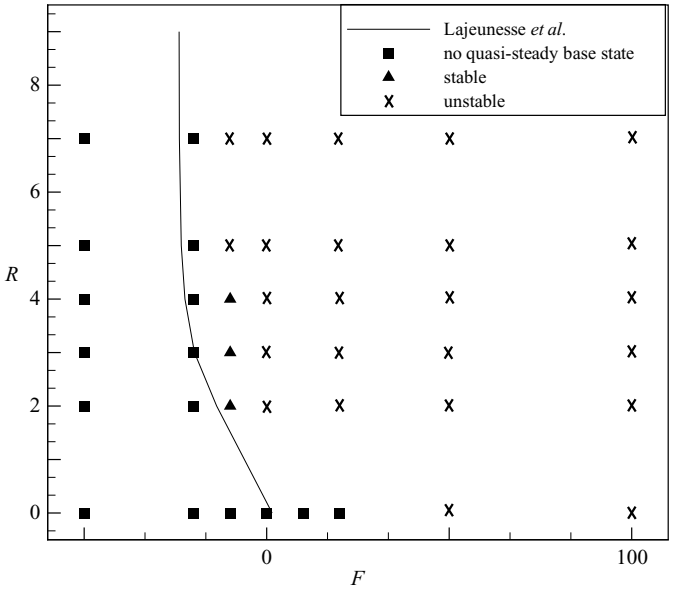

FIGURE 9. Stable and unstable regions in the (R, F)-plane for $Pe = 2000$. Comparison between present results and predictions by Lajeunesse *et al.* (1997).

positive F-values can increase the growth rate severalfold. The growth rate depends linearly on F for the range of values investigated here.

We provided a brief overview of the kinematic wave theory approach of Lajeunesse *et al.* (1999) in the limit of large Pe values in § 3.1. Lajeunesse *et al.* (1997, 2001) employ this approach to predict a critical flow velocity below which the flow is stable and primarily two-dimensional in the gap of the cell. This critical velocity in terms of their non-dimensional variables and the corresponding gravity number parameter from our scaling, is

$$U_{crit} = \frac{8\mathrm{e}^{3R}}{(4\mathrm{e}^{R} - 3)(2\mathrm{e}^{R} - 3)^{2}}, \tag{3.6}$$

$$F_{crit} = -12/U_{crit}. \tag{3.7}$$

Using this relationship, the critical value of F below which the flow is stable varies in the range $-23.9 \leqslant F \leqslant -13.7$ for $7 \geqslant R \geqslant 2$, respectively. Figure 9 provides a comparison of our numerical results with this theoretical prediction. We do not obtain steady states for $F < -10$, as indicated by the square symbols. Hence, we cannot perform a stability analysis in this regime. For smaller viscosity contrasts ($R < 5$) and $F = -10$, even though a quasi-steady state is reached, the flow is stable to spanwise perturbations. Lajeunesse *et al.* (1997) mention that (3.7) only provides a lower bound on U_{crit} for instability, and formally applies to $Pe \to \infty$. They observed an increase in U_{crit}, or correspondingly F, with Pe for $Pe < 10^4$. Since the maximum value of Pe in our stability calculations is 2000, the predictions of Lajeunesse *et al.* (1997) are consistent with the present results. In contrast to the experiments of Lajeunesse *et al.* (1997, 1999) the present numerical analysis is not restricted to gravitationally stable displacements and can explore the entire (R, F)-plane. Doing so reveals that both two-dimensional frontal shocks and three-dimensional instabilities can occur even for viscosity contrasts corresponding to $e^{R} < 1.5$, as opposed to the corresponding

experimental observations. For sufficiently strong gravitational forces, instability can occur even for constant viscosity fluids (cf. the data point for $R = 0$ and $F = 50$ in figure 9). For displacements stabilized by gravity, there exists a viscosity ratio below which the flow is always stable to three-dimensional perturbations. This viscosity ratio increases with decreasing F.

Figure 8(b) shows the dominant wavenumber for gravitationally stable displacements with $F = -10$ to be around 1.3 for $5 \leqslant R \leqslant 7$, corresponding to a wavelength of 4.8 times the gap width (note that for $R = 7$, we were unable to obtain converged results for $F > 20$). This value is substantially larger than the dominant wavelength of about three times the gap width found by Goyal & Meiburg (2006) for neutrally buoyant displacements, and it is consistent with the experimental findings of Lajeunesse *et al.* (1997). For $F > F_{crit}$, those authors had observed a dominant wavelength of 5 ± 1 times the gap width for a wide range of viscosity ratios. This weak dependence of the dominant wavelength on R for gravity-stabilized experiments is confirmed by the linear stability results. Hence, for negative F-values, the situation arises in which the instability itself is caused by the unfavourable viscosity contrast, whereas the dominant wavelength of the instability is determined by the stable density stratification.

For displacements with an unstable density stratification, the situation is opposite, in that variations in F affect the dominant wavelength only weakly, while the influence of R is much stronger. Figure 8(b) also displays another important feature. The dominant wavenumber, for unstable density stratifications, increases from $R = 0$ to $R = 2$ and subsequently decreases. Hence initially, an increase in the viscosity contrast leads to shorter wavelengths of perturbation. However, beyond $R = 2$, and for large values of F the most unstable wavelength increases with R. This is in contrast to the Rayleigh–Taylor instability in a vertical Hele-Shaw cell, for which Goyal & Meiburg (2004) found that the dominant wavelength decreases monotonically with increasing R. This demonstrates the qualitative transition between the gravitational and viscous regimes. At small values of R, even in displacement flows, wavelength selection is dictated by gravitational effects, whereas at higher viscosity contrasts, even for strongly destabilizing density differences, it is dominated by the unfavourable viscosity contrast, and not by the gravitational instability. In order to analyse the transition from gravitational to viscously dominated instability, it is instructive to analyse the eigenfunctions. Figures 10(a)–10(c) depict the concentration and spanwise velocity eigenfunction contours, along with the perturbation velocity vectors in the cross-gap plane of the Hele-Shaw cell, for $Pe = 2000$, $F = 50$ and $R = 0$. Figures 10(d)–10(f) plot the corresponding eigenfunctions for identical values of Pe and F, but with $R = 5$. A comparison of figures 10(a) and 10(d) shows that, similar to neutrally buoyant displacements, the instability still grows, centred around the tip of the displacement front. The increase in R from 0 to 5 leads to a marked reduction in the vertical extent of the concentration eigenfunctions, accompanied by a strong increase in the level of the instability (cf. figure 8a). The spanwise velocity eigenfunction for the purely gravitational instability extends across the entire gap, with a negative perturbation behind the front and a positive value ahead of the front. In contrast, for $R = 5$, the negative region of $\hat{u}$ is confined to the less viscous fluid. The viscous instability tends to create a perturbation flow across the gap, as indicated by the velocity vectors in figure 10(f), while figure 10(c) shows that the gravitational instability generates a perturbation velocity primarily aligned with the gravity vector.

A quantitative comparison of the instabilities in purely gravity-driven and displacement flows, respectively, is provided in figure 11. Shown are the growth rates

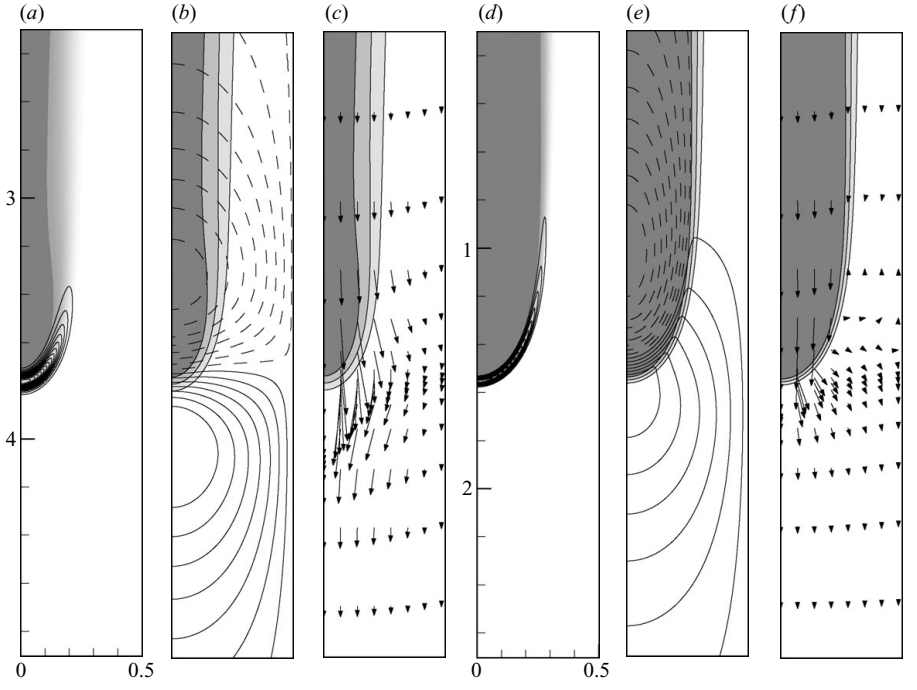

FIGURE 10. Perturbation eigenfunctions and velocity vectors for $Pe = 2000$, $F = 50$ and (*a–c*) $R = 0$, and (*d–f*) $R = 5$, superimposed on the base concentration fields provided in grey shading. (*a*, *d*) Concentration eigenfunction $\hat{c}$. (*b*, *e*) Spanwise velocity eigenfunction $\hat{u}$. (*c*, *f*) Perturbation velocity vectors in the (y, z)-plane. Solid (dashed) lines indicate positive (negative) values.

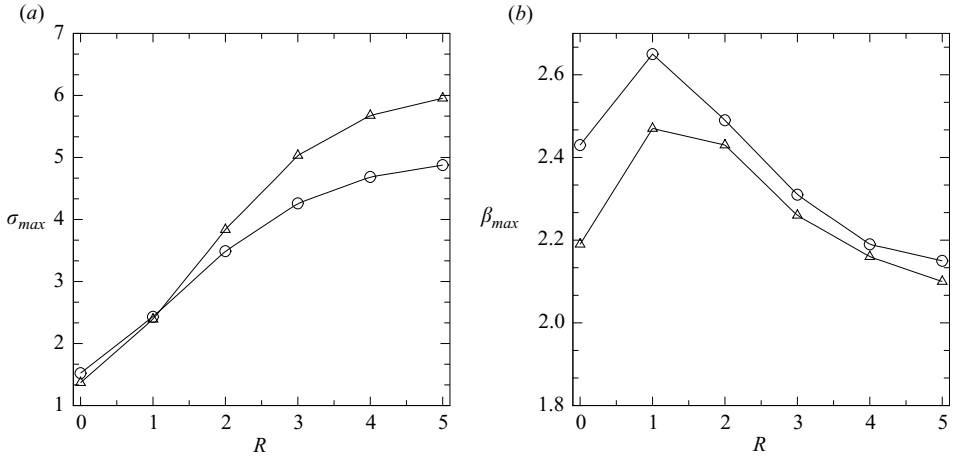

FIGURE 11. Comparison of (*a*) the growth rate, and (*b*) the wavenumber of the dominant perturbation mode as a function R, for the cases with and without a net displacement. ○, $Ra = 10^5$; △, $F = 50$, $Pe = 2000$.

and wavenumbers of the dominant mode for $Ra = 10^5$, and for the corresponding case of $Pe = 2000$ and $F = 50$. Here, the growth rates of the gravity-driven flow have been rescaled by using (3.5) between the characteristic time scales. For $R = 0$, this rescaling results in nearly identical growth rates. As the viscosity contrast between the

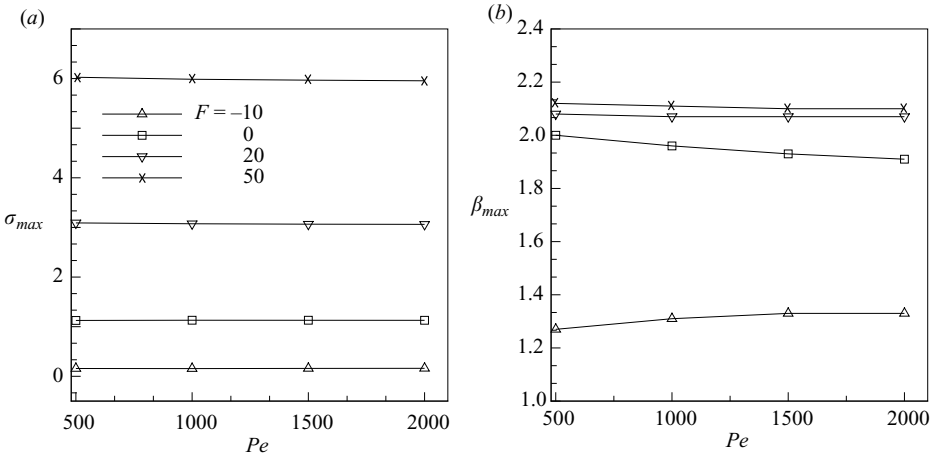

FIGURE 12. (*a*) Growth rate and (*b*) most unstable wavenumber as a function of Pe for $R = 5$ and different values of F. Both quantities depend only weakly on Pe.

two fluids is increased, the displacement flow becomes comparatively more unstable. This is consistent with our expectation, as the viscous instability reinforces the purely gravitational one. The wavelength of the dominant perturbation mode is determined largely by the viscosity ratio, as mentioned previously. The transition from a purely gravitational instability to one governed by both viscous and gravitational effects is reflected by the peak of each curve at $R = 1$.

Goyal & Meiburg (2006) showed that for neutrally buoyant displacements, the dominant wavelength increases weakly with Pe. Figure 12 plots the dominant mode growth rate and wavenumber as a function of Pe for $R = 5$ and different gravity numbers. The results indicate that in displacements governed by both viscosity and density contrasts, both the growth rate and the dominant wavenumber depend only weakly on Pe, up to $Pe = 2000$. As mentioned in Goyal & Meiburg (2006), numerical considerations prevent us from exploring higher values of Pe.

4. Discussion and conclusions

In Goyal & Meiburg (2006), we compared the growth rates and dominant wavenumbers of neutrally buoyant Stokes flow displacements with corresponding Darcy results of Tan & Homsy (1986). Bacri *et al.* (1992) and Manickam & Homsy (1995) extend the Darcy analysis to vertical flows and derive analytical dispersion relations for step concentration profiles in terms of the endpoint fluid properties. They also identify a critical displacement velocity above which the flow is unstable. We recast their relation in terms of our dimensionless parameters to obtain

$$\sigma = \frac{\beta}{24Pe}\left\{(RPe - 12\beta) + \frac{FPe}{6(1+\mathrm{e}^R)} - \sqrt{144\beta^2 + 24R\beta Pe + 4\frac{F\beta Pe}{(1+\mathrm{e}^R)}}\right\}. \quad (4.1)$$

Figure 13 shows the growth rates and dominant mode wavenumbers for both Stokes and Darcy analyses as a function of F and R for $Pe = 500$. Although the overall quantitative agreement is poor, the Darcy analysis correctly predicts an increase in the growth rate with F and R. On the other hand, it predicts a continuous strong linear increase of the dominant wavenumber with R and F, while the Stokes analysis

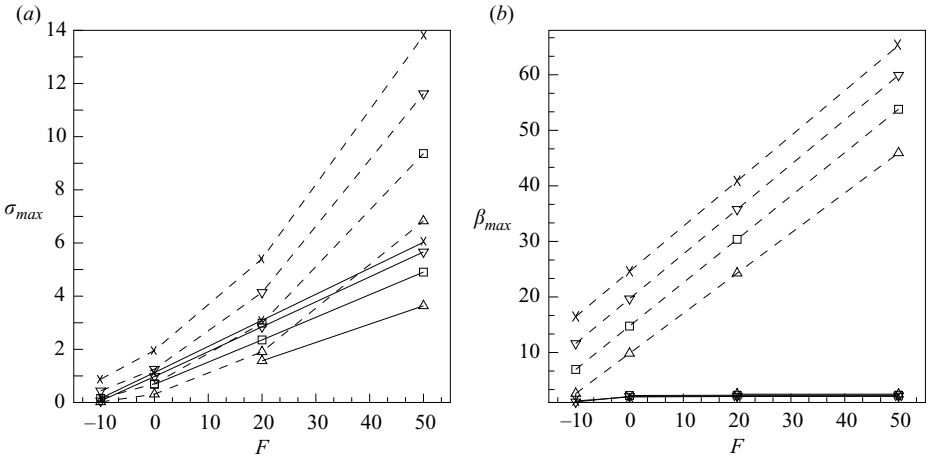

FIGURE 13. Comparison of the present Stokes flow results (solid lines) with (*a*) growth rates and (*b*) wavenumbers based on Darcy's law (dashed lines) for $Pe = 500$ and different viscosity ratios (Manickam & Homsy 1995). △; $R = 2$; □, $R = 3$; ▽, $R = 4$; ×, $R = 5$.

shows the wavenumber to depend very weakly on R, and to be nearly independent of F, for $F > 0$.

In conclusion, the Stokes flow analysis of miscible displacements in vertical Hele-Shaw cells reveals several features of the instability. For the range of parameters investigated, both the growth rate and the dominant wavenumber depend only weakly on Pe. The growth rate varies strongly, and nearly linearly, with F, so that even a moderately stable density stratification can stabilize a viscously unstable displacement. Both the growth rate and the dominant wavelength increase with the viscosity ratio R. For unstable density stratifications, the dominant wavelength is nearly independent of F. On the other hand, it increases strongly for stable density stratifications, which resolves the discrepancy between the experiments of Lajeunesse *et al.* (1997) and the analysis of neutrally buoyant displacements by Goyal & Meiburg (2006). Finally, the kinematic wave theory of Lajeunesse *et al.* (1999) is seen to capture the stability limit quite accurately, while the Darcy analysis misses important aspects of the instability.

We would like to thank B. Selvam and S. H. Vanaparthy for several helpful discussions. Support for this research was received from the NASA Microgravity and NSF/ITR programs, through an NSF equipment grant, and through TeraGrid resources provided by the San Diego Supercomputer Center.

REFERENCES

BACRI, J., SALIN, D. & YORTSOS, Y. 1992 Analyse linéaire de la stabilité de l'écoulement de fluides miscibles en milieus poreux. *C. R. Acad. Sci. Paris* **314**, 139–144.

BALASUBRAMANIAM, R., RASHIDNIA, N., MAXWORTHY, T. & KUANG, J. 2005 Instability of miscible interfaces in a cylindrical tube. *Phys. Fluids* **17** (5), 052103-1–052103-11.

CHEN, C. & MEIBURG, E. 1996 Miscible displacements in capillary tubes. Part 2. Numerical simulations. *J. Fluid Mech* **326**, 57–90.

FERNANDEZ, J., KUROWSKI, P., PETITJEANS, P. & MEIBURG, E. 2002 Density-driven unstable flows of miscible fluids in a Hele-Shaw cell. *J. Fluid Mech.* **451**, 239–260.

Goyal, N. & Meiburg, E. 2004 Unstable density stratification of miscible fluids in a vertical Hele-Shaw cell: influence of variable viscosity on the linear stability. *J. Fluid Mech.* **516**, 211–238.

Goyal, N. & Meiburg, E. 2006 Miscible displacements in Hele-Shaw cells: two-dimensional base states and their linear stability. *J. Fluid Mech.* **558**, 329–355.

Graf, F. & Meiburg, E. 2002 Density-driven instabilities of miscible fluids in a Hele-Shaw cell: linear stability analysis of the three-dimensional Stokes equations. *J. Fluid Mech.* **451**, 261–282.

Kuang, J., Maxworthy, T. & Petitjeans, P. 2003 Miscible displacements between silicone oils in capillary tubes. *Eur. J. Mech.* B/*Fluids* **22**, 271–277.

Kuang, J., Maxworthy, T. & Petitjeans, P. 2004 Velocity fields and streamline patterns of miscible displacements in cylindrical tubes. *Exps. Fluids* **37**, 301–308.

Lajeunesse, E., Martin, J., Rakotomalala, N. & Salin, D. 1997 3D instability of miscible displacements in a Hele-Shaw cell. *Phys. Rev. Lett.* **79**, 5254–5257.

Lajeunesse, E., Martin, J., Rakotomalala, N., Salin, D. & Yortsos, Y. 1999 Miscible displacement in a Hele-Shaw cell at high rates. *J. Fluid Mech.* **398**, 299–319.

Lajeunesse, E., Martin, J., Rakotomalala, N., Salin, D. & Yortsos, Y. 2001 The threshold of the instability in miscible displacements in a Hele-Shaw cell. *Phys. Fluids* **13**, 799–801.

Manickam, O. & Homsy, G. 1995 Fingering instabilities in vertical miscisble displacement flows in porous media. *J. Fluid Mech.* **288**, 75–102.

Petitjeans, P. & Maxworthy, T. 1996 Miscible displacements in capillary tubes. Part 1. Experiments. *J. Fluid Mech.* **326**, 37–56.

Tan, C. & Homsy, G. 1986 Stability of miscible displacements in porous media: rectilinear flow. *Phys. Fluids* **29** (11), 3549–3556.

Yang, Z. & Yortsos, Y. 1997 Asymptotic solutions of miscible displcements in geometries of large aspect ratio. *Phys. Fluids* **9** (2), 286–298.